Laser feedback interferometry in multi-mode terahertz quantum cascade lasers

Xiaoqiong Qi,[1] **Gary Agnew,**[1] **Thomas Taimre,**[2] **She Han,**[1] **Yah Leng Lim,**[1] **Karl Bertling,**[1] **Aleksandar Demić,**[3] **Paul Dean,**[3] **Dragan Indjin,**[3] **and Aleksandar D. Rakić**[1,*]

[1]*School of Information Technology and Electrical Engineering, The University of Queensland, Brisbane, QLD 4072, Australia*
[2]*School of Mathematics and Physics, The University of Queensland, Brisbane, QLD 4072, Australia*
[3]*School of Electronic and Electrical Engineering, University of Leeds, Leeds LS2 9JT, UK*
[*]*rakic@itee.uq.edu.au*

Abstract: The typical modal characteristics arising during laser feedback interferometry (LFI) in multi-mode terahertz (THz) quantum cascade lasers (QCLs) are investigated in this work. To this end, a set of multi-mode reduced rate equations with gain saturation for a general Fabry-Pérot multi-mode THz QCL under optical feedback is developed. Depending on gain bandwidth of the laser and optical feedback level, three different operating regimes are identified, namely a single-mode regime, a multi-mode regime, and a tuneable-mode regime. When the laser operates in the single-mode and multi-mode regimes, the self-mixing signal amplitude (peak to peak value of the self-mixing fringes) is proportional to the feedback coupling rate at each mode frequency. However, this rule no longer holds when the laser enters into the tuneable-mode regime, in which the feedback level becomes sufficiently strong (the boundary value of the feedback level depends on the gain bandwidth). The mapping of the identified feedback regimes of the multi-mode THz QCL in the space of the gain bandwidth and feedback level is investigated. In addition, the dependence of the aforementioned mapping of these three regimes on the linewidth enhancement factor of the laser is also explored, which provides a systematic picture of the potential of LFI in multi-mode THz QCLs for spectroscopic sensing applications.

1. Introduction

Since terahertz (THz) quantum cascade lasers (QCLs) were first successfully demonstrated in 2002 [1], the development of THz QCL technology has witnessed remarkable growth over the past 17 years. THz QCLs can now emit > 2.4 W output power in pulsed mode [2] and > 130 mW in cw [3] within the 1.2–5.6 THz range [4–7], and operate at temperatures of up to 210 K in pulsed mode [8] and 129 K in cw [9]. Moreover, the multi-stack active region design with its emission spectrum centered at different frequencies [10–12] provides an effective way to broaden the spectral gain bandwidth [full width at half-maximum (FWHM)] of THz QCLs up to 1.1 THz [13].

Laser feedback interferometry (LFI) utilizing THz QCLs has been investigated comprehensively over the past decade and has established itself as one of the most promising technologies for sensing and imaging applications in this part of the electromagnetic spectrum [14–22]. In a typical LFI system, the laser emission from the THz QCL reflects back into the laser cavity from an external target, mixes with the intra-cavity electric field, and generates a measurable self-mixing (SM) signal in both the emission power and terminal voltage of the laser [20]. As a coherent sensing technique, LFI technology has the capacity to provide both amplitude and phase

information about the external target or the external cavity without the need for external detectors, which is very attractive at THz frequencies for which existing detectors are either not sufficiently sensitive or are not fast enough, such as pyroelectric detectors or Golay cells, respectively [22]. In addition, the SM signal in THz QCLs is typically two orders of magnitude larger than that in laser diodes (LDs) [23] with high detection sensitivity [24]. Consequently, THz QCL-based LFI technology has been demonstrated for a wide variety of applications, including high-resolution THz imaging [23,25], three-dimensional image reconstruction [26,27], biomedical imaging [28,29], and materials analysis [30–32].

Most of the reported THz QCL-based LFI systems have employed a single-mode THz QCL. However, a wide range of biomedical tissues and chemicals have a characteristic spectrum which often contains multiple "spectral fingerprints" in the THz region [33,34]. Frequency tuneability in coupled-cavity THz QCLs has been demonstrated theoretically and experimentally [35,36], and applications of multi-spectral terahertz sensing have also been proposed [37], where a set of SM signals at multiple THz frequencies could be obtained through tuning the driving current applied on the passive cavity of the laser. More conveniently than LFI in a coupled-cavity THz QCL, LFI in a single-cavity multi-mode THz QCL has been demonstrated to measure the emission spectrum of the device itself [38], which offers a simple alternative to Fourier transform infrared (FTIR) spectroscopy approaches typically employed for spectral characterization of mid- and far-infrared lasers. With an external cavity extension of 200 mm, a frequency resolution of 750 MHz has been achieved in that work, which in principle could be further improved to less than 15 MHz with further cavity extension up to 10 m. By using the same principle, gas spectroscopy has been demonstrated in a multi-mode THz QCL [39]. In that work, spectral features of methanol at two longitudinal modes at 3.362 THz and 3.428 THz were measured simultaneously. Although multi-spectral sensing with LFI in a multi-mode THz QCL has been experimentally demonstrated, the optical feedback effects in a multi-mode THz QCL are not yet fully understood.

All current theoretical studies of THz laser-feedback interferometers are based on the assumption of single-mode QCLs. A model for a pulsed THz QCL under optical feedback was proposed and the interplay between electro-optical, thermal, and feedback phenomena was investigated to understand the laser behavior [40]. In [41], it was concluded that the high value of the photon to carrier lifetime ratio and the negligible linewidth enhancement factor determines the ultrastable of QCLs against optical feedback. In addition, the multi-mode instability threshold of the stationary emission of a QCL with optical feedback was studied [42] where it should be noted the multi-mode regimes in that work refers to external cavity modes rather than laser cavity longitudinal modes. The laser behavior in a multi-longitudinal-mode (indicated as multi-mode in the following sections) THz QCL under optical feedback are very different from that of the single-mode case, due to mode competition of the optical gain in the active region of the laser created by stimulated emission through transitions of the injected carriers. Indeed, it is much more complicated than single-mode case when optical feedback occurs between reflected multi-mode and intra-cavity modes in a multi-mode THz QCL, which results in mode cooperation or mode suppression, depending on optical feedback conditions.

It should be pointed out that mode instabilities, including spatial hole burning (SHB) [43] and Risken-Nummedal-Graham-Haken (RNGH) [44] have been demonstrated dominant in multi-longitudinal-mode THz QCLs due to fast gain recovery. They could lead to a proliferation of modes with random phases and destroy coherence. The influence of SHB in mode-locked QCLs were emphasized since it can reduce pulse duration and deteriorate pulse quality [45,46]. However, SHB was not clearly observed experimentally in a multi-mode THz QCL under feedback when it was used for multi-spectral applications as mentioned above [38,39], to a large extent due to the laser is driven very close to its threshold current to maximize self-mixing signal. For the multi-spectral sensing applications, the steady-state Lang-Kobayashi model [47] has been used to

analyze the self-mixing signal properties in multi-mode THz QCLs with optical feedback [19,38] where it was assumed that different laser modes operated independently in the Fabry-Pérot (FP) resonator of the THz QCL.

In this work, we explore the characteristics of a FP multi-mode THz QCL under optical feedback and investigate the boundary feedback conditions within which the multi-mode THz QCL could be used for multi-spectral sensing applications. Multi-mode reduced rate equations (RREs) model have been successfully used for the prediction of mode switching dynamics in coupled-cavity THz QCLs with and without optical feedback [35,37,48]. Here we improved the multi-mode RREs model by introducing gain saturation at each of the longitudinal modes. Depending on the optical feedback level and gain spectral bandwidth, three typical feedback regimes are identified, which are the single-mode regime, the multi-mode regime, and the tuneable-mode regime. In single-mode and multi-mode regimes, the SM signal amplitude at each mode is proportional to the feedback coupling coefficient at that particular frequency. Since the feedback coupling coefficients are determined by the coupling factor, reflection coefficients, and phase shift induced by the target, the LFI technology could be used for measurements of the absorption coefficient and complex refractive index of the media in the external cavity or of the target itself. More importantly, the dependence of the absorption coefficient and complex refractive index within a range of THz frequencies can be extracted directly from the multi-mode SM amplitude by extending the external cavity length when the laser operates in the multi-mode regime. However, unlike the single-mode and multi-mode cases, the amplitude of the SM signal is no longer proportional to the feedback coupling coefficient when the feedback is sufficiently strong that the laser enters into tuneable-mode regime. This suggests that a multi-mode laser operating in the tuneable-mode regime cannot be used for spectroscopic sensing directly via the external cavity extension method. However, it could be used as a tuneable laser for spectroscopic sensing when combined with current sweeping for SM signal generation [30].

In addition to the above, a second-order amplitude modulation on the SM signal at the optical path length of the laser cavity is investigated for the laser operating in all these three regimes. This phenomenon could be used to extract the actual lasing cavity length or the effective refractive index of the laser if one of these two is known. The mapping of the feedback regimes of the multi-mode THz QCL in the space of the gain spectral bandwidth and feedback level is investigated as well. The influence of the linewidth enhancement factor on the feedback regime mapping is also explored, which indicates that a multi-mode THz QCL with a larger linewidth enhancement factor has larger multi-mode regime that could be used for spectroscopic sensing.

The remainder of this article is organized as follows. Section 2 describes the multi-mode RRE model in the presence of optical feedback for a multi-mode THz QCL and the analytical expression of the SM signal derived from single-mode RREs. This is followed by an exploration of SM signal characteristics in different feedback regimes in multi-mode THz QCLs in Sec. 3.1 and Sec. 3.2. The feedback regime mappings in the space of feedback level and gain bandwidth, and its dependence on the linewidth enhancement factor are presented in Sec. 3.3. Finally, Sec. 4 presents our conclusions.

2. Theoretical model of LFI in multi-mode THz QCLs

The exemplar device selected for simulation is based on a GaAs/AlGaAs bound-to-continuum active region structure as described in Ref. [49]. The wafer was grown on a semi-insulating GaAs substrate by molecular beam epitaxy and processed into a surface plasmon ridge waveguide using optical lithography and wet chemical etching at University of Leeds, UK . A standard FP type THz QCL without external feedback normally lases on multiple longitudinal modes with the mode spacing determined by $c/(2n_{in}L_{in})$, where n_{in} and L_{in} are the refractive index and laser cavity length of the laser, respectively. We consider a laser feedback interferometer in such a single-cavity multi-mode THz QCL as shown schematically in Fig. 1. We considered

seven central longitudinal modes from Mode 1 (M1) to Mode 7 (M7) which have the material gain larger than the total loss in the laser cavity at each of the mode frequencies to demonstrate emission mode structure changes due to optical feedback condition varying. The multi-mode THz beam emitted from the laser transmits through the external cavity and reflected from the external target with the reflection coefficient $R(\nu)$ and phase change $\theta_R(\nu)$ respectively, which are generally frequency (ν) dependent. The electric field sustained within the laser cavity mixes with the reinjected field from the target at each mode frequency and causes measurable changes in the total emission power and terminal voltage. The variations in the emission power and terminal voltage contain information of the reflection coefficient and phase change of the target, as well as the external cavity optical path length and re-injection loss. These variations are also influenced by some of the laser intrinsic parameters, such as linewidth enhancement factor, photon and electron lifetimes, number of the active region stages, and electron injection efficiencies, as shown below. The absorption spectrum of the target (or the media in the external cavity) can be extracted from the variations in the emission power or terminal voltage of the multi-mode THz QCL which are induced by optical feedback from an extending external cavity length. Nevertheless, this only occurs when the optical feedback condition is appropriate under which the modes are co-existing and the SM signal characteristics are not changed due to mode competition.
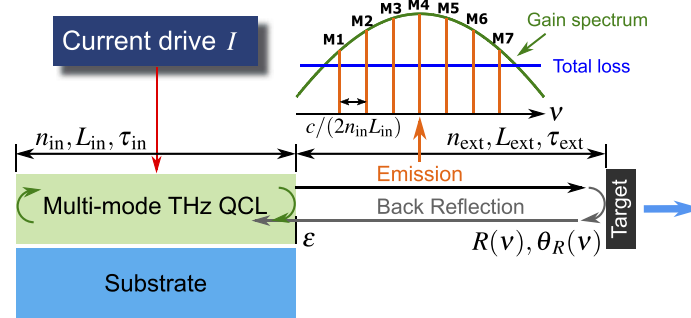
Fig. 1. Laser feedback interferometry model for a multi-mode THz QCL. The laser cavity has refractive index n_{in} and cavity length L_{in} with corresponding internal cavity round trip time τ_{in}. Seven longitudinal modes from Mode 1 (M1) to Mode 7 (M7) which have the material gain larger than the total loss in the laser cavity are considered in this work. This multi-mode emission is transmitted through the facet on the right-hand side of the laser cavity and traverses the external cavity of refractive index n_{ext} and length L_{ext} with corresponding external cavity round trip time τ_{ext} before reflecting back toward the QCL from the target. The power reflectivity and phase change introduced by the target are $R(\nu)$ and $\theta_R(\nu)$ respectively, which are generally frequency dependent. A portion of the reflected light, dictated by the re-injection coupling factor ε, re-enters the laser and mixes with the field inside the laser cavity, generating a set of SM signals at multi-mode frequencies through extending external cavity length with a moving target, which can be used to extract $R(\nu)$ and $\theta_R(\nu)$.

In order to fully explore the characteristics of the SM signal at each mode in multi-mode THz QCLs, we used the following set of multi-mode RREs, which is a updated version of the multi-mode RREs [35,37,48] by involving gain saturation in gain factor at each mode:

$$\frac{dN_3(t)}{dt} = \frac{\eta_3 I}{q} - \sum_{m=1}^{N} G_m \left(N_3(t) - N_2(t)\right) S_m(t) - \frac{N_3(t)}{\tau_3}, \tag{1}$$

$$\frac{dN_2(t)}{dt} = \frac{\eta_2 I}{q} + \sum_{m=1}^{N} G_m \left(N_3(t) - N_2(t)\right) S_m(t) + \frac{N_3(t)}{\tau_{32}} + \frac{N_3(t)}{\tau_{sp}} - \frac{N_2(t)}{\tau_2}, \tag{2}$$

$$\frac{\mathrm{d}S_m(t)}{\mathrm{d}t} = MG_m(N_3(t) - N_2(t))\, S_m(t) + M\frac{\beta_{\mathrm{sp}}}{\tau_{\mathrm{sp}}} N_3(t) - \frac{S_m(t)}{\tau_{\mathrm{p},m}}$$

$$\underbrace{+ \frac{2\kappa}{\tau_{\mathrm{in}}}\, (S_m(t)S_m(t-\tau_{\mathrm{ext}}))^{\frac{1}{2}}\, \cos\left(2\pi\nu_{\mathrm{r},m}\tau_{\mathrm{ext}} + \phi_m(t) - \phi_m(t-\tau_{\mathrm{ext}})\right)}_{\text{Feedback Term}} \qquad (3)$$

$$m = 1, 2, \ldots, N,$$

$$\frac{\mathrm{d}\phi_m(t)}{\mathrm{d}t} = \frac{\alpha}{2}\left(MG_m(N_3(t) - N_2(t)) - \frac{1}{\tau_{\mathrm{p},m}}\right)$$

$$\underbrace{- \frac{\kappa}{\tau_{\mathrm{in}}}\left(\frac{S_m(t-\tau_{\mathrm{ext}})}{S_m(t)}\right)^{\frac{1}{2}}\, \sin\left(2\pi\nu_{\mathrm{r},m}\tau_{\mathrm{ext}} + \phi_m(t) - \phi_m(t-\tau_{\mathrm{ext}})\right)}_{\text{Feedback Term}} \qquad (4)$$

$$m = 1, 2, \ldots, N,$$

where $N_3(t)$ and $N_2(t)$ are the carrier populations in the upper and lower laser levels (ULL/LLL) of the active cavity, respectively, while $S_m(t)$ and $\phi_m(t)$ represent the photon population and the phase of the electric field in mode m. Equations (3) and (4) each represent N equations for the photon population and the phase for each of the longitudinal eigen-mode. The electron transport parameters $(\eta_3, \eta_2, \tau_3, \tau_2, \tau_{32})$ are obtained from full self-self-consistent energy-balance Schrödinger–Poisson scattering transport calculations for the given driving current I described in Refs. [40,50–52]. The driving current of the multi-mode laser is a constant at 0.75 A during external cavity extension process so that the dependence of the input parameters on the voltage and temperature can be ignored.

The initial eigen-mode frequencies of the multi-mode THz QCL that are determined by the optical path in the laser cavity are updated at each time step by solving the set of phase rate Eq. (4) which in turn are used in the set of electron population and photon population rate Eqs. (1), (2), and (3). The entire set of the RREs is solved numerically using the fourth-order Runge–Kutta method. Once the equations are solved, the emission output power per mode can be calculated by $P_m(t) = \eta_{0,m}\hbar\omega_m S_m(t)/\tau_{\mathrm{p},m}$, where $\eta_{0,m} = \alpha_{\mathrm{m},m}/2/(\alpha_\mathrm{a} + \alpha_{\mathrm{m},m})$ is power output coupling coefficient for mode m [53]. However, the dependence of the feedback coupling coefficient κ on mode frequencies has been neglected to investigate the influence of the gain spectrum on the emission mode structure. The photon lifetime $\tau_{\mathrm{p},m}$ is calculated from $\tau_{\mathrm{p},m} = (v_{\mathrm{g},m}(\alpha_\mathrm{a} + \alpha_{\mathrm{m},m}))^{-1}$, where $\alpha_{\mathrm{m},m} = \ln(r_{1,m}r_{2,m})^{-1}/L_{\mathrm{in}}$ is the mirror loss of the laser cavity at mode m, and $r_{1,m} = r_{2,m} = (n_{\mathrm{in}}(\nu_m) - 1)/(n_{\mathrm{in}}(\nu_m) + 1)$ is the reflectivities of the laser facets. α_a is the waveguide loss (the dependence on frequency has been neglected) and $v_{\mathrm{g},m} = c/n_{\mathrm{in}}(\nu_m)$ is the group velocity for mode m.

In order to gain a better understanding of the characteristics of the SM signal, we determined the steady state solutions of the carrier populations and the emission power that all contain an SM signal from the single-mode RREs when $m = 1$ in Eqs. (1)–(4). Defining the rate at which reinjected light is coupled into the laser cavity as $\widetilde{\kappa} = \kappa/\tau_{\mathrm{in}}$, and neglecting spontaneous emission terms and gain compression effect, the steady state solutions are given by

$$N_{2\mathrm{s}} = \frac{1}{A}\left(\frac{I}{q}(\eta_2 + \eta_3) + \left(\frac{1}{\tau_2} - A\right)B\right), \qquad (5)$$

$$N_{3\mathrm{s}} = N_{2\mathrm{s}} + B, \qquad (6)$$

$$S_\mathrm{s} = \frac{1}{BG_0}\left(\frac{\eta_3 I}{q} - \frac{N_{3\mathrm{s}}}{\tau_3}\right), \qquad (7)$$

where $A = \tau_2^{-1} - \tau_{32}^{-1} - \tau_{sp}^{-1} + \tau_3^{-1}$, $B = MG_0^{-1}\left(\tau_p^{-1} - 2\widetilde{\kappa}\cos(\phi_{FB})\right)$, and all the other symbols have their usual meanings. It should be noted that here G_0 is the gain factor of the single-mode, which is chosen at the peak gain frequency.

When $2\widetilde{\kappa}\tau_p\cos(\phi_{FB}) \ll 1$, the photon population can be further derived:

$$S_s = S_{2s}(2\widetilde{\kappa}\tau_p)^2\cos^2(\phi_{FB}) + S_{1s}2\widetilde{\kappa}\tau_p\cos(\phi_{FB}) + (S_{1s} - S_{2s}), \quad (8)$$

where $S_{2s} = (G_0A\tau_3\tau_2)^{-1}$, $S_{1s} = (\eta_3IM\tau_p)q^{-1} - (\eta_3 + \eta_2)IM\tau_p(qA\tau_3)^{-1}$, and ϕ_{FB} is the steady state phase under optical feedback. The term ϕ_{FB} in turn satisfies the *excess phase equation* [20]:

$$\phi_{FB} - \phi_s + C\sin(\phi_{FB} + \arctan\alpha) = 0. \quad (9)$$

Accordingly, Eqs. (5) and (6) can be rewritten as:

$$N_{2s} = \frac{\tau_2A - 1}{\tau_2AMG_0}2\widetilde{\kappa}\cos(\phi_{FB}) + \frac{1 - \tau_2A}{\tau_2AMG_0\tau_p} + \frac{I(\eta_2 + \eta_3)}{qA} \quad (10)$$

$$N_{3s} = -\frac{1}{\tau_2AMG_0}2\widetilde{\kappa}\cos(\phi_{FB}) + \frac{1}{\tau_2AMG_0\tau_p} + \frac{I(\eta_2 + \eta_3)}{qA}. \quad (11)$$

The steady-state photon population as shown in Eq. (8) contains three terms: DC component $S_{1s} - S_{2s}$, first-order AC component $S_{1s}2\widetilde{\kappa}\tau_p\cos(\phi_{FB})$ and second-order AC component $S_{2s}(2\widetilde{\kappa}\tau_p)^2\cos^2(\phi_{FB})$. It is observed from Eq. (8) that, although physically the photon population is defined as the square of the electric field, namely, $S(t) = |E(t)|^2$ [20], mathematically the dominant term of S_s is the first-order AC component term $S_{1s}2\widetilde{\kappa}\tau_p\cos(\phi_{FB})$, which is proportional to the electric field due to the definition of the feedback coupling rate $\widetilde{\kappa}$. The SM amplitude, which is defined as the peak-to-peak values of the SM fringes, is mainly determined by $S_{1s}2\widetilde{\kappa}\tau_p$. Furthermore, the feedback coupling rate is proportional to the square root of the target reflectivity $\sqrt{R}$ and the re-injection coupling factor ε. Therefore, when the target is probed by a multi-mode THz beam at a group of THz frequencies, the SM signal at each frequency, which contains the reflectivity and the phase change at each particular frequency, can serve as a "fingerprint" to extract the refractive index at multiple THz frequencies of the target. This has clear application in material identification. It is also noted that the first-order AC component of S_s is not influenced by the gain factor. However, the larger the gain factor, the larger the DC component of the S_s, but the weaker the second-order AC component term of S_s. Nevertheless, the SM amplitude contained in carrier populations are influenced by the gain factor, as shown in first terms of Eqs. (10) and (11). The larger the gain factor, the smaller the SM amplitude on both N_{2s} and N_{3s}.

It is worth pointing out that the SM amplitude is influenced by the gain factor at each mode frequency in multi-mode THz QCLs due to mode competition of the optical gain. As shown in Sec. 3.1, the mode with highest gain factor has highest SM amplitude. Therefore, a flat gain spectrum for multi-mode THz QCLs would be preferred for spectroscopic sensing applications. Multi-stack THz QCLs provide just such a broadened gain spectral bandwidth for such applications [10–12]. The simultaneous influence of gain bandwidth and optical feedback level on the SM signal characteristics in multi-mode THz QCLs is investigated in Sec. 3.

The gain saturation at high photon populations and the associated gain compression coefficient ε_g is taken into account in the model to avoid emission energy being overly concentrated on the central mode in the gain spectrum. The gain compression coefficient ε_g for photon populations in a multi-mode THz QCL can be estimated by:

$$\varepsilon_g = \frac{\hbar\omega_m v_g}{I_{s,m}V} = \frac{c^3\tau_3}{4\pi n_{in}^5 V\tau_{sp}v_{r,m}^2\Delta\nu} \quad (12)$$

where $I_{s,m}$ is the saturation intensity for mode m [54] and V is the active region volume. The meaning of other symbols, together with typical values used in the simulations are summarized in

Table 1. It is noted that the key parameters which influence the modal characteristics or the side mode suppression ratio (SMSR) of the multi-mode emission include the spontaneous lifetime τ_{sp}, the linewidth enhancement factor α, and active region refractive index dispersion $n_{in}(\nu_m)$. By choosing reasonable values for the parameters above for THz QCLs as shown in Table 1, and when the multi-mode RREs are solved forward in time domain to their steady state, the values of the gain compression coefficient had to be chosen to be two orders of magnitude larger than the

Table 1. Parameters used in Eq. (1)–(12) for the THz QCL model.

Symbol	Description	Value / Units
η_3	Injection efficiency into ULL	54 %
η_2	Injection efficiency into LLL	1.65 %
I	Drive current	0.75 A
L_{in}	Laser cavity length	3 mm
M	Number of periods in active cavity	90
β_{sp}	Spontaneous emission factor	1.627×10^{-4}
τ_3	Total carrier lifetime in ULL	5×10^{-12} s
τ_{32}	Non-radiative relaxation time from ULL to LLL	1.76×10^{-10} s
τ_2	Total carrier lifetime in LLL	2.1×10^{-11} s
τ_{sp}	Spontaneous emission lifetime	1×10^{-6} s
α_a	Waveguide loss of active cavity	9 cm^{-1}
$\nu_{r,m}$	Emission frequency with no optical feedback	2.712, 2.725, 2.738, 2.752, 2.765, 2.778, 2.791 THz
ν_m	Emission frequency with optical feedback	Varies
G_m	Gain factor for mode m, from mode 1 to 7	See note[a]
G_0	Peak gain factor	1.8×10^4 s^{-1}
ε_g	Gain compression coefficient for photon population	$9.1667 \times 10^{-6} \times 800\,\text{GHz}/\Delta\nu$
ν_p	Peak gain frequency	2.752 THz
$\Delta\nu$	Full width at half maximum (FWHM) of the gain spectrum	Varies
τ_{ext}	Initial round-trip time of the external cavity, $\tau_{ext} = 2L_{ext}n_{ext}/c$	3.336×10^{-9} s
L_{ext}	Initial external cavity length	0.5 m
n_{ext}	Refractive index of external cavity	1.00
$n_{in}(\nu_m)$	Group refractive index of active region at Mode 1 to 7 frequencies	3.6114, 3.6121, 3.6129, 3.6137, 3.6144, 3.6152, 3.6159
κ	Feedback coupling coefficient, $\kappa = \varepsilon\sqrt{R/R_2}(1 - R_2)$	Varies
$\widetilde{\kappa}$	Feedback coupling rate, $\widetilde{\kappa} = \kappa/\tau_{in}$	Varies
ε	Re-injection coupling factor	Varies
R_2, R	Reflectivity of right laser facet and external target	0.5662 and 0.7
α	Henry's linewidth enhancement factor	-0.1
C	Feedback parameter, $C = \widetilde{\kappa}\tau_{ext}\sqrt{1 + \alpha^2}$	Varies
ϵ_0	Vacuum permittivity	8.854×10^{-12} F m^{-1}
q	Elementary charge	1.602×10^{-19} C
c	Speed of light in vacuum	299792458 m s^{-1}

[a]Varies as $G_m = G_0/(1 + ((\nu_p - \nu_{r,m})/(\Delta\nu/2))^2)/(1 + (\varepsilon_g S_m(t)))$.

estimated value from (12) to allow multi-mode emission. This may be partially explained by the fact that we neglect the symmetric cross gain saturation from neighboring modes [55,56] and the spatial hole burning effect [57] in the model.

3. Results and discussion

3.1. Typical modal characteristics in multi-mode THz QCLs

The emission power from a multi-mode THz QCL under optical feedback contains a set of SM signals at multi-mode THz frequencies. The set of SM signals is created by extending the length of the external cavity from an initial value for L_{ext} of 0.5 m, as illustrated in Fig. 1. The shape of the SM temporal waveform at each mode and consequently the emission spectrum from the multi-mode THz QCL is determined by both the gain spectrum of the laser and the level of optical feedback. The emission power at each mode was calculated by solving the set of RREs with fourth-order Runge–Kutta method at each external cavity length for 2 µs to reach temporal steady state. In order to investigate changes of the SM signal waveform at each mode, the external cavity length was extended by an amount ΔL_{ext} of 250 µm with a step size of 2 µm in this section. It should be noted that we used three modifications as follows to speed up (in silico) the dynamical process as in order to reach the temporal steady state with reduced computational effort: 1) we solved the rate equation for the mode frequency with optical feedback v_m instead of the mode phase $\phi_m(t)$ to avoid its accumulation with the time, considering that $d\phi_m(t)/dt = 2\pi(v_m - v_{r,m})$; 2) the optical feedback terms in the rate equations of photon population and the frequency at each mode were replaced by their steady state versions as $(2\kappa/\tau_{in})S_m(t)\cos(2\pi v_m\tau_{ext})$ and $-(\kappa/\tau_{in})\sin(2\pi v_m\tau_{ext})$, respectively [20]; 3) the photon and carrier populations were normalized (divided) by 10^6 so that they are on the same order of magnitude as the mode frequency. Depending on the gain spectrum bandwidth and optical feedback level, a multi-mode THz QCL with an extending external cavity can exhibit characteristics of either a single-mode laser, a multi-mode laser, or a tuneable laser.

Narrow gain spectrum bandwidth usually leads to large SMSR in the multi-mode emission power, and we defined the modal structure to be single-mode when SMSR of the THz emission power between the strongest two modes are larger than 30 dB. As shown in Fig. 2(a), when the gain bandwidth (FWHM) Δv is 360 GHz with the re-injection coupling factor ε of 0.001(C=0.0228), the SMSR between Mode 4 and 5 is around 50 dB, indicating single-mode emission. The emission power at each of the modes as a function of varying ΔL_{ext} is shown on both a logarithmic and linear scale in Fig. 2(a) and Fig. 2(b), respectively, for the purpose of illustrating the typical modal structure and visualization of the SM signal amplitude at each mode, respectively. The logarithmic scale is good to show the definition of the modal structure but fails to clearly display the vast difference in the SM signal amplitude for each of the modes due to nonlinear amplification of the values larger and smaller than 1. Around 4.5 SM fringes generated due to the external cavity extension ΔL_{ext} of 250 µm can be observed from the insets of Fig. 2(b) on Mode 4, 5, and 3 with decreasing SM amplitude from 3 µW, 0.0258 µW, to 0.00214 µW as a result of frequency dependent gain factor. The DC component of emission power at Mode 4, 5, and 3 are 6.59 mW, 0.157 µW, and 0.0528 µW, respectively. In this scenario, most of the gain contributes to the central mode frequency (Mode 4). Although the SM signal is carried on each of the longitudinal modes, the DC component of the side modes are too weak to be used for spectroscopic sensing applications.

The SM signal amplitude at each mode increases with increasing feedback level as observed from Eq. (1). When the SMSR reduces to 30 dB and smaller, the laser emission exhibits multi-mode modal structure. To show a typical multi-mode SM signal waveform with the coexistance of effective emission power at more than two modes, the simulation result with the gain bandwidth Δv of 800 GHz and the re-injection coupling factor ε of 0.001 ($C = 0.0228$) is given in Fig. 3, with the SMSR among the two strongest modes only 3.45 dB. The SM amplitude
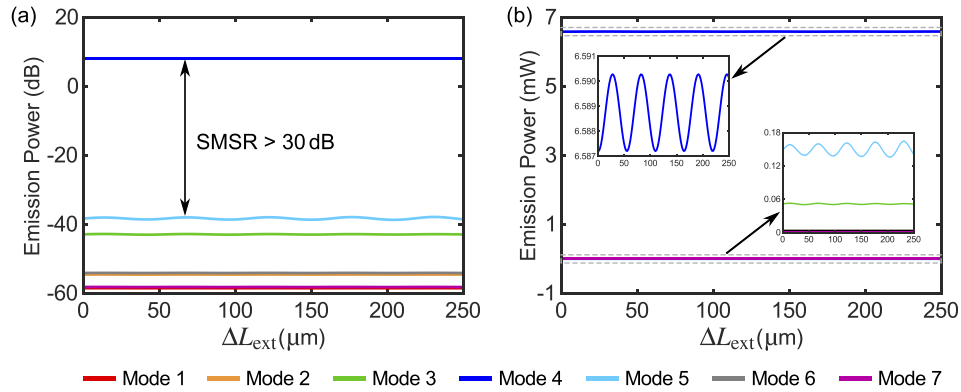
Fig. 2. Emission from a multi-mode THz QCL under optical feedback specified here results in SMSR > 30 dB and practically single-mode operation. The parameters used in the simulation are as follows: $L_{ext} = 0.5$ m, $R = 0.7$, $\Delta\nu = 360$ GHz, and $\varepsilon = 0.001(C = 0.0228)$. (a) The emission power as a function of ΔL_{ext} on a logarithmic scale, which is used to define the single-mode scenario with SMSR > 30 dB. (b) The emission power on a linear scale, which is used to easily visualization the relationship between the SM signal amplitude at each mode.

at Mode 4, 5, and 3 are 0.108 mW, 0.0780 mW, and 0.0287 mW, respectively at the DC component of emission power of 4.51 mW, 1.98 mW, and 0.111 mW. In this regime, since there is more than one mode that has relatively large DC emission power and AC component of the SM signal, it can be used for spectroscopic sensing to measure the absorption "fingerprints" at multiple THz frequencies [38,39]. The asymmetry in the modal emission power of Mode 3 and 5 is due to refractive index dispersion, which also leads to higher output coupling coefficient for Mode 5 compared to Mode 3. Since the amplitude of SM signal depends on both the feedback coupling coefficient κ and the gain factor G_m at each mode frequency ν_m, the emission spectrum obtained
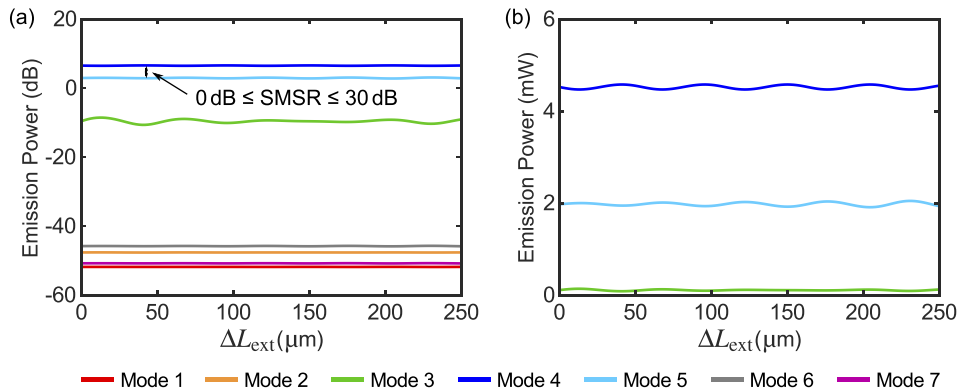
Fig. 3. Emission from a multi-mode THz QCL under optical feedback specified here results in 0 dB $\leq$ SMSR ≤ 30 dB and practically multi-mode operation. The parameters used in the simulation are as follows: $L_{ext} = 0.5$ m, $R = 0.7$, $\Delta\nu = 800$ GHz, and $\varepsilon = 0.001(C = 0.0228)$. (a) The emission power as a function of ΔL_{ext} on a logarithmic scale, which is used to define the multi-mode scenario to be when the smallest 0 dB $\leq$ SMSR ≤ 30 dB. (b) The emission power on a linear scale, which is used to easily visualization the relationship between the SM signal amplitude at each mode.

by performing a Fourier transform of the total emission power, couples the gain spectrum of the laser and is influenced by the feedback level. By choosing a proper reference target with known reflection coefficient, the multi-mode regime can be used to measure the reflection coefficient spectrum for an unknown target [39]. When the influence of the gain factor on the SM amplitude at each mode is removed by using the reference target, SM signal amplitude will be proportional to the reflection coefficient of the target under study in the multi-mode regime.

When the optical feedback level is further increased, the multi-mode THz QCL enters into the tuneable mode region, where the mode competition is so strong that only part of the set of LFI-induced fringes for each mode remains; most of the SM fringes are suppressed by other modes, which leads to mode switching. As shown in Fig. 4, when the re-injection coupling factor ε increases to 0.1 ($C = 2.283$) with a gain bandwidth $\Delta\nu$ of 800 GHz, mode switching among Mode 4(3), 5, 6, 7 and 2 occurs cyclically when pulling back the target every half wavelength. The relationships between the gain spectrum and the position of the eigen-mode frequencies on the threshold gain spectrum (which is determined by the feedback parameters), determines the next dominant mode with varying ΔL_{ext}, which hops to the mode with the largest net gain. In this regime, the SM signal amplitude is on the order of mW, which is much larger than that for single- and multi-mode cases, and is not proportional to the feedback coupling coefficient κ anymore.
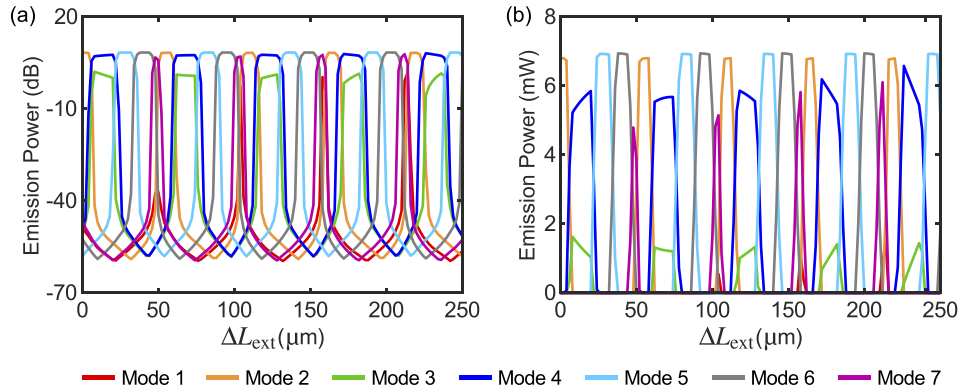
Fig. 4. Emission from a multi-mode THz QCL under optical feedback specified here results in any of the SMSRs between Mode 4 and other modes < 0 dB and practically tuneable-mode operation. The parameters used in the simulation are as follows: $L_{ext} = 0.5$ m, $R = 0.7$, $\Delta\nu = 800$ GHz, and $\varepsilon = 0.1(C = 2.283)$. (a) The emission power as a function of ΔL_{ext} on a logarithmic scale, which is used to define the tuneable-mode scenario with SMSR between Mode 4 and other modes are negative in dB. (b) The emission power on a linear scale as a function of ΔL_{ext}.

3.2. Laser cavity modulations on the SM signal in multi-mode THz QCLs

In addition to the periodic modulation on the emission power with the SM fringes which occurs on the order of a half wavelength on each mode frequencies discussed in Sec. 3.1, it is found that there is additional modulation phenomenon which occurs on the order of optical path in the intra-laser cavity in the emission power of each mode, as shown in Fig. 5. This longer amplitude modulation occurring periodically with the external cavity extensions of around $n_{in}(\nu_m)L_{in}$, which are 10.8342 mm, 10.8364 mm, 10.8387 mm, 10.8410 mm, 10.8432 mm, 10.8455 mm, 10.8477 mm, respectively for each of the modes. It is also worth pointing out that this laser cavity modulation on the emission power is a universal phenomenon no matter whether the laser is operating in single-mode regime, multi-mode regime, or tuneable-mode regime, which are demonstrated in Fig. 5 (a), (b), and (c), respectively. This phenomenon is induced by light wave

propagating and reflected by the laser facets in intra-laser cavity and could be used to measure the actual lasing cavity length in a single-mode or multi-mode THz QCL if the refractive index of the active region material is known or vice versa. This phenomenon was also observed in multi-mode LDs [58].
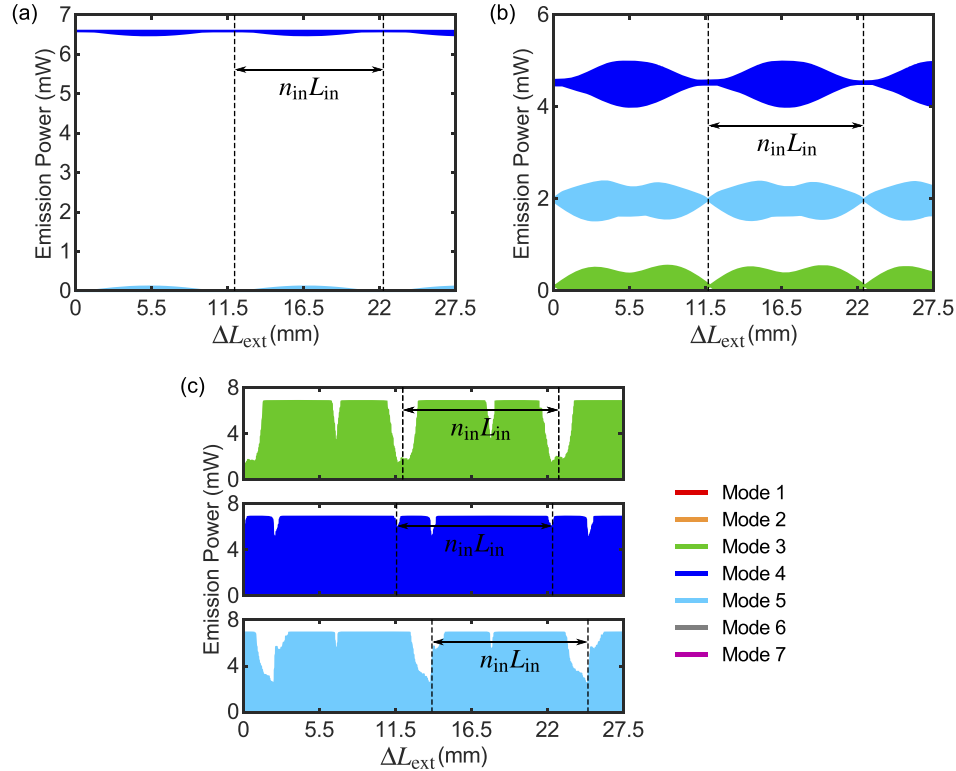
Fig. 5. The laser cavity modulation on the emission power in the multi-mode THz QCL with the extending external cavity length of 27.5 mm for (a) single-mode operation, (b) multi-mode operation, and (c) tuneable-mode operation. The longer amplitude modulation on the optical path in the laser cavity of $n_{in}L_{in}$ are observed in all three cases.

3.3. Mapping of the three regimes from LFI in multi-mode THz QCLs

Considering a Lorenzian gain spectrum centered at Mode 4 (the central mode), we simulated the multi-mode SM waveforms with external cavity extendsion with varying gain spectral bandwidth and feedback coupling coefficient ε, and calculate the SMSR between the central mode (Mode 4) and the other modes accordingly. The regime is defined as tuneable mode region when any of the SMSRs between the central mode and other modes is negative, which means there is mode switching during the target pull back process. Otherwise, it is defined as single-mode regime or multi-mode regime if the minimum of the SMSR between the central mode and other modes is larger or smaller than 30 dB, respectively. We indicate the single-mode regime, multi-mode regime, and tuneable-mode regime as Regime 1, 2, 3, respectively in the feedback regime maps in Fig. 6. We choose 100×20 equispaced points for the feedback coupling coefficient ε varying from 0 to 0.2 and the gain bandwidth varying from 100 GHz to 1100 GHz in the mapping. For each point in the map, we solve the RREs for 2 μs at each external target position and external cavity extension of $n_{in}L_{in}$ of 10.85mm with a step of 2 μm. For the purpose of multi-spectral sensing applications, the interesting feedback condition is in the range of weak and moderate

feedback levels defined for single-mode LDs with the corresponding feedback parameter C varying from 0 to 4.566 for a THz QCL if the initial external cavity length was used to calculate C (same applys for the values of C mentioned below) [20].
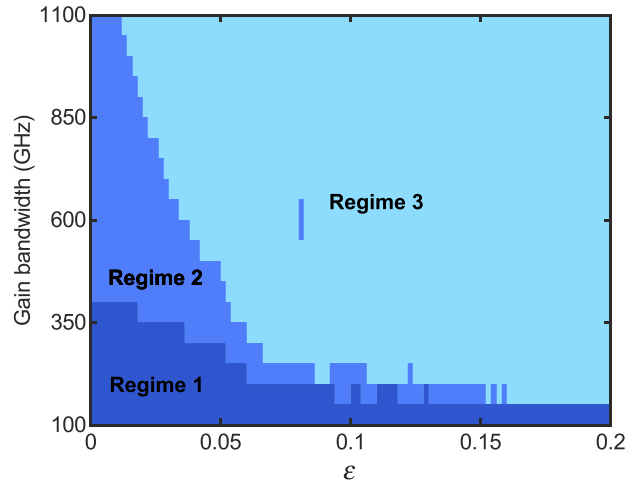
Fig. 6. The feedback regime map in the space of the gain spectral bandwidth and feedback coupling coefficient ε ($0 \leq C \leq 4.566$) when $L_{ext} = 0.5$ m and $\alpha = -0.1$, where Regime 1, 2, and 3 refer to the single-mode regime, multi-mode regime, and tuneable-mode regime, respectively.

When the gain bandwidth is too narrow (< 150 GHz with the intrinsic laser parameters chosen in Table 1), the laser exhibits high stability to feedback perturbations so that it is always in single-mode regime with no influence by optical feedback due to limited optical gain, as shown in Fig. 6. However, if the laser has a moderate gain bandwidth between 150 GHz to around 400 GHz, although it is still single-mode in the absence of optical feedback (the line when $\varepsilon = 0$ in Fig. 6), it transits to multi-mode with growing feedback level. For example, the laser with gain bandwidth of 300 GHz enters into multi-mode regime when $\varepsilon = 0.04$ ($C = 0.913$). The phenomenon that mode structures of SM waveform changes from single-mode to multi-mode with increasing optical feedback level was observed experimentally in LDs and THz QCLs as well [38,59], which leads to subperiodicity in the shape of the SM waveform. As mentioned in Sec. 3.1, there are two routes to enter into the multi-mode regime: increasing feedback level for a fixed gain bandwidth or increasing the gain bandwidth for a fixed feedback level, which can be clearly observed from the regime mappings in Fig. 6. The SMSR is decreasing with the growing feedback level until it is below zero that the laser enters into tuneable mode regime when ε is larger than 0.064 ($C = 1.461$), as shown in Fig. 7. The value of ε when the laser transits from multi-mode regime (Regime 2) to tuneable-mode regime (Regime 3) is decreasing with increasing gain bandwith. When the gain bandwidth is larger than 400 GHz, the laser is multi-mode without optical feedback, and the SMSR is decreasing with increasing feedback level until the laser enters into tuneable mode regime. For example, when gain bandwidth is 500 GHz, the laser becomes tunealbe-mode when ε is around 0.042 ($C = 0.959$), and it reduces to 0.012 ($C = 0.274$) when the gain bandwidth increases to 1000 GHz. Therefore, although broad gain bandwidth has less gain spectrum influence on spectroscopic sensing spectrum extraction, the multi-mode regime that can be used for this application is smaller. The tiny region of Regime 2 (multi-mode regime) in the Regime 3 (tuneable-mode regime) in Fig. 6 is due to changes of SMSR from negative to positive values smaller than 1 dB, which is the definition of the boundary condition between multi-mode and tuneable-mode regime. Although the single-mode THz

QCL with intermediate optical feedback has been demonstrated for gas sensing recently [60], multi-mode THz QCL with intermediate optical feedback is hardly used for sensing applications due to mode competition.
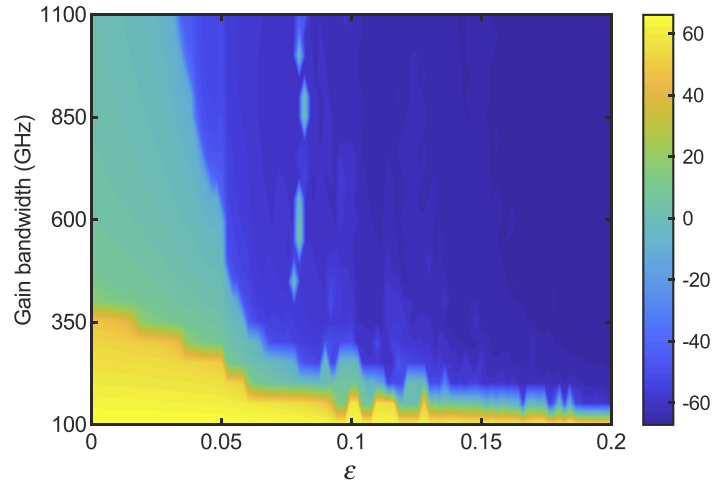
Fig. 7. The side-mode suppression ratio (SMSR) map in the space of the gain spectral bandwidth and feedback coupling coefficient ε when $L_{ext} = 0.5$ m and $\alpha = -0.1$ ($0 \leq C \leq 4.566$), where the units of the SMSR values beside the colorbar are dB.
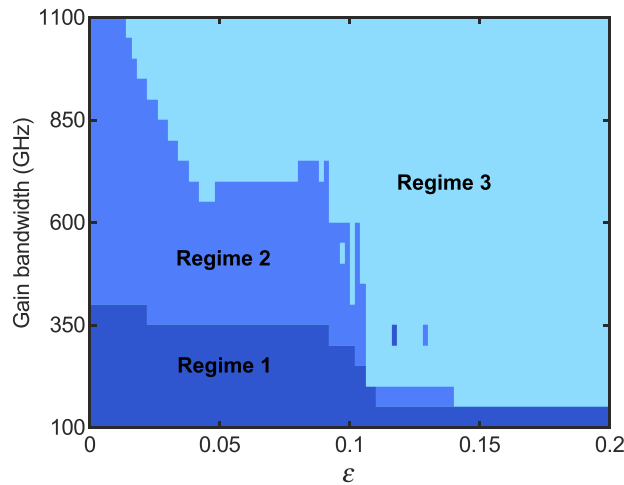
Fig. 8. The feedback regime map in the space of the gain spectral bandwidth and feedback coupling coefficient ε ($0 \leq C \leq 5.080$) when $L_{ext} = 0.5$ m and $\alpha = 0.5$, where Regime 1, 2, and 3 refer to the single-mode regime, multi-mode regime, and tuneable-mode regime, respectively.

The regime mapping with a increased linewidth enhancement factor of 0.5 in the space of gain bandwidth and feedback coupling coefficient ε ($0 \leq C \leq 5.080$) is shown in Fig. 8 with the SMSR mapping in the same space shown in Fig. 9. It is observed that the multi-mode regime (Regime 2) is broadened with larger linewidth enhancement factor due to that the SMSR is increasing with increasing linewidth enhancement factor for the fixed gain bandwidth and feedback level, which gives more tolerence to optical feedback before the transition to tuneable-mode regime and makes

the multi-mode regime larger. This suggests that FP THz QCLs with larger linewidth enhancement factor have more tolerance to optical feedback level that can be used for spectroscopic sensing due to larger multi-mode regime.
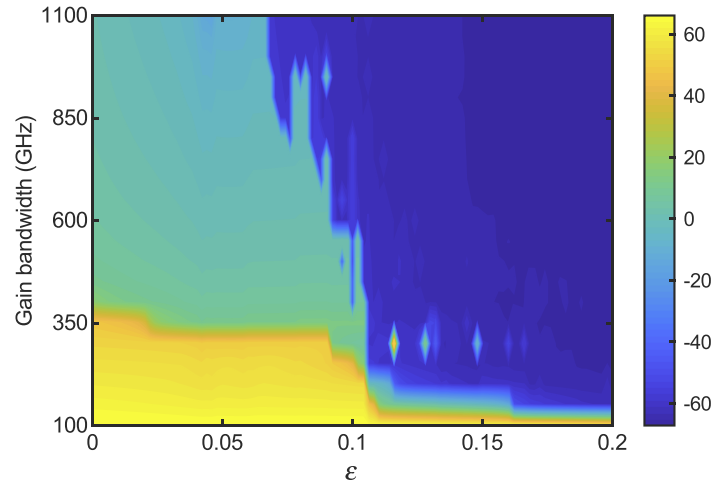
Fig. 9. The side-mode suppression ratio (SMSR) map in the space of the gain spectral bandwidth and feedback coupling coefficient ε ($0 \leq C \leq 5.080$) when $L_{ext} = 0.5$ m and $\alpha = 0.5$, where the units of the SMSR values beside the colorbar are dB.

4. Conclusion

In conclusion, we explored the general characteristics of a FP multi-mode THz QCL under optical feedback through developing an original theoretical model that involves multi-mode RREs and gain saturation. The emission modal structure which contains a set of SM signals at each of the mode frequencies is determined by both gain spectrum of the laser and the optical feedback levels.

By varying optical feedback level and gain bandwidth, we identified three typical operation regimes, which includes a single-mode, a multimode, and a tuneable-mode regime, depending on the gain bandwidth and optical feedback levels. We discovered that only the multi-mode regime with a set of SM signals whose amplitudes are proportional to the reflection coefficient of the target at each of the THz frequencies could be used for spectroscopic sensing. The feedback regime map of the investigated modal structures in the space of gain spectral bandwidth and feedback level is also explored. The results provide design criteria for multi-mode THz QCLs when they are used for spectroscopic sensing in terms of the operating feedback level at varying gain bandwidth. The regime map with larger linewidth enhancement factor suggests that the multi-mode regime extended into higher feedback levels and would give more tolerance to optical feedback when used for spectroscopic sensing at the same gain bandwidth.

Acknowledgements

Disclosures

The authors declare that there are no conflicts of interest related to this article.

References

1. R. Köhler, A. Tredicucci, F. Beltram, H. E. Beere, E. H. Linfield, A. G. Davies, D. A. Ritchie, R. C. Iotti, and F. Rossi, "Terahertz semiconductor-heterostructure laser," Nature **417**(6885), 156–159 (2002).
2. L. Li, L. Chen, J. Freeman, M. Salih, P. Dean, A. Davies, and E. Linfield, "Multi-watt high-power THz frequency quantum cascade lasers," Electron. Lett. **53**(12), 799–800 (2017).
3. B. S. Williams, S. Kumar, Q. Hu, and J. L. Reno, "High-power terahertz quantum cascade lasers," in *2006 Conference on Lasers and Electro-Optics and 2006 Quantum Electronics and Laser Science Conference*, (2006), pp. 1–2.
4. G. Scalari, C. Walther, M. Fischer, R. Terazzi, H. Beere, D. Ritchie, and J. Faist, "THz and sub-THz quantum cascade lasers," Laser Photonics Rev. **3**(1-2), 45–66 (2009).
5. C. W. I. Chan, Q. Hu, and J. L. Reno, "Ground state terahertz quantum cascade lasers," Appl. Phys. Lett. **101**(15), 151108 (2012).
6. M. Wienold, B. Röben, X. Lü, G. Rozas, L. Schrottke, K. Biermann, and H. T. Grahn, "Frequency dependence of the maximum operating temperature for quantum-cascade lasers up to 5.4 THz," Appl. Phys. Lett. **107**(20), 202101 (2015).
7. L. Li, I. Kundu, P. Dean, E. H. Linfield, and A. G. Davies, "High-power GaAs/AlGaAs quantum cascade lasers with emission in the frequency range 4.7–5.6 THz," in *International Quantum Cascade Lasers School and Workshop*, (Cambridge, UK, 2016).
8. L. Bosco, M. Franckié, G. Scalari, M. Beck, A. Wacker, and J. Faist, "Thermoelectrically cooled thz quantum cascade laser operating up to 210 K," Appl. Phys. Lett. **115**(1), 010601 (2019).
9. M. Wienold, B. Röben, L. Schrottke, R. Sharma, A. Tahraoui, K. Biermann, and H. T. Grahn, "High-temperature, continuous-wave operation of terahertz quantum-cascade lasers with metal-metal waveguides and third-order distributed feedback," Opt. Express **22**(3), 3334–3348 (2014).
10. C. Gmachl, D. L. Sivco, R. Colombelli, F. Capasso, and A. Y. Cho, "Ultra-broadband semiconductor laser," Nature **415**(6874), 883–887 (2002).
11. D. Turčinková, G. Scalari, F. Castellano, M. I. Amanti, M. Beck, and J. Faist, "Ultra-broadband heterogeneous quantum cascade laser emitting from 2.2 to 3.2 THz," Appl. Phys. Lett. **99**(19), 191104 (2011).
12. M. Rösch, G. Scalari, M. Beck, and J. Faist, "Octave-spanning semiconductor laser," Nat. Photonics **9**(1), 42–47 (2015).
13. D. Bachmann, M. Rösch, C. Deutsch, M. Krall, G. Scalari, M. Beck, J. Faist, K. Unterrainer, and J. Darmo, "Spectral gain profile of a multi-stack terahertz quantum cascade laser," Appl. Phys. Lett. **105**(18), 181118 (2014).
14. Y. L. Lim, P. Dean, M. Nikolić, R. Kliese, S. P. Khanna, M. Lachab, A. Valavanis, D. Indjin, Z. Ikonić, P. Harrison, E. H. Linfield, A. G. Davies, S. J. Wilson, and A. D. Rakić, "Demonstration of a self-mixing displacement sensor based on terahertz quantum cascade lasers," Appl. Phys. Lett. **99**(8), 081108 (2011).
15. F. P. Mezzapesa, L. L. Columbo, M. Dabbicco, M. Brambilla, and G. Scamarcio, "QCL-based nonlinear sensing of independent targets dynamics," Opt. Express **22**(5), 5867–5874 (2014).
16. P. Dean, A. Valavanis, J. Keeley, K. Bertling, Y. L. Lim, R. Alhathlool, A. D. Burnett, L. H. Li, S. P. Khanna, D. Indjin, T. Taimre, A. D. Rakić, E. H. Linfield, and A. G. Davies, "Terahertz imaging using quantum cascade lasers — a review of systems and applications," J. Phys. D: Appl. Phys. **47**(37), 374008 (2014).
17. T. Hagelschuer, N. Rothbart, H. Richter, M. Wienold, L. Schrottke, H. T. Grahn, and H.-W. Hübers, "High-spectral-resolution terahertz imaging with a quantum-cascade laser," Opt. Express **24**(13), 13839–13849 (2016).
18. M. Wienold, T. Hagelschuer, N. Rothbart, L. Schrottke, K. Biermann, H. Grahn, and H.-W. Hübers, "Real-time terahertz imaging through self-mixing in a quantum-cascade laser," Appl. Phys. Lett. **109**(1), 011102 (2016).
19. T. Hagelschuer, M. Wienold, H. Richter, L. Schrottke, K. Biermann, H. Grahn, and H.-W. Hübers, "Terahertz gas spectroscopy through self-mixing in a quantum-cascade laser," Appl. Phys. Lett. **109**(19), 191101 (2016).
20. T. Taimre, M. Nikolić, K. Bertling, Y. L. Lim, T. Bosch, and A. D. Rakić, "Laser feedback interferometry: a tutorial on the self-mixing effect for coherent sensing," Adv. Opt. Photon. **7**(3), 570–631 (2015).
21. K. S. Reichel, S. Biasco, T. Crisci, K. Garrasi, F. P. Mezzapesa, and M. S. Vitiello, "Self-mixing interferometry in continuous-wave high power 1D and 2D QCL random lasers operating at terahertz frequencies," in *2019 44th International Conference on Infrared, Millimeter, and Terahertz Waves (IRMMW-THz)*, (2019), pp. 1–2.
22. A. Rakić, T. Taimre, K. Bertling, Y. L. Lim, P. Dean, A. Valavanis, and D. Indjin, "Sensing and imaging using laser feedback interferometry with quantum cascade lasers," Appl. Phys. Rev. **6**(2), 021320 (2019).

23. P. Dean, Y. L. Lim, A. Valavanis, R. Kliese, M. Nikolić, S. P. Khanna, M. Lachab, D. Indjin, Z. Ikonić, P. Harrison, A. D. Rakić, E. H. Linfield, and A. G. Davies, "Terahertz imaging through self-mixing in a quantum cascade laser," Opt. Lett. **36**(13), 2587–2589 (2011).

24. J. Keeley, K. Bertling, P. Rubino, Y. L. Lim, T. Taimre, X. Qi, I. Kundu, L. Li, D. Indjin, A. Rakić, E. H. Linfield, A. G. Davies, J. Cunningham, and P. Dean, "Detection sensitivity of laser feedback interferometry using a terahertz quantum cascade laser," Opt. Lett. **44**(13), 3314–3317 (2019).

25. M. Ravaro, V. Jagtap, G. Santarelli, C. Sirtori, L. Li, S. P. Khanna, E. H. Linfield, and S. Barbieri, "Continuous-wave coherent imaging with terahertz quantum cascade lasers using electro-optic harmonic sampling," Appl. Phys. Lett. **102**(9), 091107 (2013).

26. P. Dean, A. Valavanis, J. Keeley, K. Bertling, Y. L. Lim, R. Alhathlool, S. Chowdhury, T. Taimre, L. Li, D. Indjin, S. J. Wilson, A. D. Rakić, E. H. Linfield, and A. Giles Davies, "Coherent three-dimensional terahertz imaging through self-mixing in a quantum cascade laser," Appl. Phys. Lett. **103**(18), 181112 (2013).

27. J. Keeley, P. Dean, A. Valavanis, K. Bertling, Y. L. Lim, R. Alhathlool, T. Taimre, L. Li, D. Indjin, A. Rakić, E. H. Linfield, and A. G. Davies, "Three-dimensional terahertz imaging using swept-frequency feedback interferometry with a quantum cascade laser," Opt. Lett. **40**(6), 994–997 (2015).

28. Y. L. Lim, T. Taimre, K. Bertling, P. Dean, D. Indjin, A. Valavanis, S. P. Khanna, M. Lachab, H. Schaider, T. W. Prow, H. P. Soyer, S. J. Wilson, E. H. Linfield, A. G. Davies, and A. D. Rakić, "High-contrast coherent terahertz imaging of porcine tissue via swept-frequency feedback interferometry," Biomed. Opt. Express **5**(11), 3981–3989 (2014).

29. A. D. Rakić, G. Agnew, X. Qi, T. Taimre, Y. L. Lim, K. Bertling, S. Han, S. J. Wilson, A. Grier, I. Kundu, L. Li, A. Valavanis, P. Dean, Z. Ikonić, J. Cooper, S. P. Khanna, M. Lachab, E. H. Linfield, A. G. Davies, P. Harrison, and D. Indjin, "Terahertz frequency quantum cascade lasers: Optical feedback effects and applications," in *2016 International Conference on Numerical Simulation of Optoelectronic Devices (NUSOD)*, (2016), pp. 203–204.

30. A. D. Rakić, T. Taimre, K. Bertling, Y. L. Lim, P. Dean, D. Indjin, Z. Ikonić, P. Harrison, A. Valavanis, S. P. Khanna, M. Lachab, S. J. Wilson, E. H. Linfield, and A. G. Davies, "Swept-frequency feedback interferometry using terahertz frequency QCLs: a method for imaging and materials analysis," Opt. Express **21**(19), 22194–22205 (2013).

31. T. Taimre and A. D. Rakić, "On the nature of Acket's characteristic parameter C in semiconductor lasers," Appl. Opt. **53**(5), 1001–1006 (2014).

32. S. Han, K. Bertling, P. Dean, J. Keeley, A. D. Burnett, Y. L. Lim, S. P. Khanna, A. Valavanis, E. H. Linfield, A. G. Davies, D. Indjin, T. Taimre, and A. D. Rakić, "Laser feedback interferometry as a tool for analysis of granular materials at terahertz frequencies: Towards imaging and identification of plastic explosives," Sensors **16**(3), 352 (2016).

33. L. Ho, M. Pepper, and P. Taday, "Terahertz spectroscopy: Signatures and fingerprints," Nat. Photonics **2**(9), 541–543 (2008).

34. G. P. Kniffin, S. Schecklman, J. Chen, S. C. Henry, L. M. Zurk, B. Pejcinovic, and A. I. Timchenko, "Measurement and modeling of terahertz spectral signatures from layered material," *Proc. SPIE 7687, Active and Passive Signatures* (2010), p. 768708.

35. X. Qi, I. Kundu, P. Dean, G. Agnew, T. Taimre, A. Valavanis, A. T. Grier, E. H. Linfield, A. G. Davies, D. Indjin, and A. D. Rakić, "Mode selection and tuning mechanisms in coupled-cavity terahertz quantum cascade lasers," IEEE J. Sel. Top. Quantum Electron. **23**(4), 1–12 (2017).

36. I. Kundu, P. Dean, A. Valavanis, L. Chen, L. Li, J. E. Cunningham, E. H. Linfield, and A. G. Davies, "Quasi-continuous frequency tunable terahertz quantum cascade lasers with coupled cavity and integrated photonic lattice," Opt. Express **25**(1), 486–496 (2017).

37. X. Qi, G. Agnew, I. Kundu, T. Taimre, Y. L. Lim, K. Bertling, P. Dean, A. Grier, A. Valavanis, E. H. Linfield, A. G. Davies, D. Indjin, and A. D. Rakić, "Multi-spectral terahertz sensing: proposal for a coupled-cavity quantum cascade laser based optical feedback interferometer," Opt. Express **25**(9), 10153–10165 (2017).

38. J. Keeley, J. Freeman, K. Bertling, Y. L. Lim, R. A. Mohandas, T. Taimre, L. H. Li, D. Indjin, A. D. Rakić, E. H. Linfield, A. G. Davies, and P. Dean, "Measurement of the emission spectrum of a semiconductor laser using laser-feedback interferometry," Sci. Rep. **7**(1), 7236 (2017).

39. Y. Han, J. Partington, R. Chhantyal-Pun, M. Henry, O. Auriacombe, T. Rawlings, L. Li, J. Keeley, M. Oldfield, N. Brewster, R. Dong, P. Dean, A. G. Davies, B. N. Ellison, E. H. Linfield, and A. Valavanis, "Gas spectroscopy through multimode self-mixing in a double-metal terahertz quantum cascade laser," Opt. Lett. **43**(24), 5933–5936 (2018).

40. G. Agnew, A. Grier, T. Taimre, Y. L. Lim, K. Bertling, Z. Ikonić, A. Valavanis, P. Dean, J. Cooper, S. P. Khanna, M. Lachab, E. H. Linfield, A. G. Davies, P. Harrison, D. Indjin, and A. D. Rakić, "Model for a pulsed terahertz quantum cascade laser under optical feedback," Opt. Express **24**(18), 20554–20570 (2016).

41. F. P. Mezzapesa, L. L. Columbo, M. Brambilla, M. Dabbicco, S. Borri, M. S. Vitiello, H. E. Beere, D. A. Ritchie, and G. Scamarcio, "Intrinsic stability of quantum cascade lasers against optical feedback," Opt. Express **21**(11), 13748–13757 (2013).

42. L. Columbo and M. Brambilla, "Multimode regimes in quantum cascade lasers with optical feedback," Opt. Express **22**(9), 10105–10118 (2014).

43. A. Gordon, C. Y. Wang, L. Diehl, F. X. Kärtner, A. Belyanin, D. Bour, S. Corzine, G. Höfler, H. C. Liu, H. Schneider, T. Maier, M. Troccoli, J. Faist, and F. Capasso, "Multimode regimes in quantum cascade lasers: From coherent instabilities to spatial hole burning," Phys. Rev. A **77**(5), 053804 (2008).

44. N. Vukovic, J. Radovanovic, V. Milanovic, and D. L. Boiko, "Analytical expression for risken-nummedal-graham-haken instability threshold in quantum cascade lasers," Opt. Express **24**(23), 26911–26929 (2016).

45. V.-M. Gkortsas, C. Wang, L. Kuznetsova, L. Diehl, A. Gordon, C. Jirauschek, M. A. Belkin, A. Belyanin, F. Capasso, and F. X. Kärtner, "Dynamics of actively mode-locked quantum cascade lasers," Opt. Express **18**(13), 13616–13630 (2010).

46. S. Shimu, A. Docherty, M. Talukder, and C. Menyuk, "Suppression of spatial hole burning and pulse stabilization for actively modelocked quantum cascade lasers using quantum coherent absorption," J. Appl. Phys. **113**(5), 053106 (2013).

47. R. Lang and K. Kobayashi, "External optical feedback effects on semiconductor injection laser properties," IEEE J. Quantum Electron. **16**(3), 347–355 (1980).

48. I. Kundu, F. Wang, X. Qi, H. Nong, P. Dean, J. R. Freeman, A. Valavanis, G. Agnew, A. T. Grier, T. Taimre, L. H. Li, D. Indjin, J. Mangeney, J. Tignon, S. S. Dhillon, A. D. Rakić, J. E. Cunningham, E. H. Linfield, and A. G. Davies, "Ultrafast switch-on dynamics of frequency-tuneable semiconductor lasers," Nat. Commun. **9**(1), 3076 (2018).

49. S. Barbieri, J. Alton, H. E. Beere, J. Fowler, E. H. Linfield, and D. A. Ritchie, "2.9 THz quantum cascade lasers operating up to 70 K in continuous wave," Appl. Phys. Lett. **85**(10), 1674–1676 (2004).

50. P. Harrison and A. Valavanis, *Quantum Wells, Wires and Dots: Theoretical and Computational Physics of Semiconductor Nanostructures* (Wiley, 2016).

51. V. Jovanović, S. Höfling, D. Indjin, N. Vukmirović, Z. Ikonić, P. Harrison, J. Reithmaier, and A. Forchel, "Influence of doping density on electron dynamics in GaAs/ AlGaAs quantum cascade lasers," J. Appl. Phys. **99**(10), 103106 (2006).

52. G. Agnew, A. Grier, T. Taimre, Y. L. Lim, M. Nikolić, A. Valavanis, J. Cooper, P. Dean, S. P. Khanna, M. Lachab, E. H. Linfield, A. G. Davies, P. Harrison, Z. Ikonić, D. Indjin, and A. D. Rakić, "Efficient prediction of terahertz quantum cascade laser dynamics from steady-state simulations," Appl. Phys. Lett. **106**(16), 161105 (2015).

53. L. A. Coldren, S. W. Corzine, and M. L. Mashanovitch, *Diode lasers and photonic integrated circuits* (John Wiley & Sons, 2012).

54. A. Yariv, *Quantum Electronics* (Wiley, 1982).

55. M. Yamada, "Theoretical analysis of nonlinear optical phenomena taking into account the beating vibration of the electron density in semiconductor lasers," J. Appl. Phys. **66**(1), 81–89 (1989).

56. M. Ahmed, M. Yamada, and S. Abdulrhmann, "A multimode simulation model of mode-competition low-frequency noise in semiconductor lasers," Fluct. Noise Lett. **01**(03), L163–L170 (2001).

57. D. Lenstra and M. Yousefi, "Rate-equation model for multi-mode semiconductor lasers with spatial hole burning," Opt. Express **22**(7), 8143–8149 (2014).

58. P. J. De Groot, "Range-dependent optical feedback effects on the multimode spectrum of laser diodes," J. Mod. Opt. **37**(7), 1199–1214 (1990).

59. M. Ruiz-Llata and H. Lamela, "Self-mixing technique for vibration measurements in a laser diode with multiple modes created by optical feedback," Appl. Opt. **48**(15), 2915–2923 (2009).

60. T. Hagelschuer, M. Wienold, H. Richter, L. Schrottke, H. T. Grahn, and H.-W. Hübers, "Real-time gas sensing based on optical feedback in a terahertz quantum-cascade laser," Opt. Express **25**(24), 30203–30213 (2017).